nature astronomy

Article

https://doi.org/10.1038/s41550-025-02746-w

A possible challenge for cold and warm dark matter

Received: 16 September 2025

Accepted: 13 November 2025

Published online: 05 January 2026

Check for updates

Simona Vegetti[1] ✉, Simon D. M. White[1], John P. McKean[2,3,4], Devon M. Powell[1], Cristiana Spingola[5], Davide Massari[6], Giulia Despali[6,7,8] & Christopher D. Fassnacht[9]

Measuring the density profile and mass concentration of dark-matter haloes is a key test of the standard cold dark matter paradigm. Such objects are dark and thus challenging to characterize, but they can be studied via gravitational lensing. Recently, a million-solar-mass object was discovered superposed on an extended and extremely thin gravitational arc. Here we report on extensive tests of various assumptions for the mass density profile and redshift of this object. We find that models that best describe the data have two components: an unresolved point mass of radius ≤10 pc centred on an extended mass distribution with an almost constant surface density out to a truncation radius of 139 pc. These properties do not resemble any known astronomical object. However, if the object is dark matter dominated, its structure is incompatible with cold dark matter models but may be compatible with a self-interacting dark-matter halo where the central region has collapsed to form a black hole. This detection could thus carry substantial implications for our current understanding of dark matter.

Dark matter makes up 85% of cosmic matter, but its nature is still unknown. The cold dark matter (CDM) paradigm, in which dark matter consists of massive non-relativistic, collisionless elementary particles, agrees well with a wide variety of astrophysical observations. However, it remains largely untested on sub-galactic scales. One prediction of this model is that cosmic structure formed through a hierarchical bottom-up process. As a result, a large population of low-mass dark-matter haloes (down to planetary mass scales) is expected to exist both (1) as sub-haloes in massive galaxy and cluster haloes and (2) in the field, with mass functions and mass density profiles that have been well characterized through extensive numerical simulations (see, for example, ref. 1). Modifications of CDM in which dark-matter particles have a non-negligible thermal velocity at early times (that is, warm dark matter (WDM)) can predict orders of magnitude fewer low-mass haloes, and these have significantly less concentrated mass density profiles (see, for example, refs. 2,3). The reduction of the number of haloes and their concentration is directly related to the mass of the WDM particle.

Self-interacting dark matter (SIDM), where the particles have both gravitational and non-gravitational interactions, can redistribute energy and momentum within haloes, modifying their dark-matter distribution and thus creating more diverse density profiles than in CDM (see, for example, refs. 4–8). If the self-interaction cross-section is high enough, haloes can evolve to have a highly concentrated density profile at the centre. Such objects form via a runaway contraction process, known as the gravo-thermal catastrophe, or core collapse[9–11], and can be considerably more centrally concentrated than CDM haloes of the same mass. Core collapse rapidly leads to the formation of a central black hole, which, unlike in CDM models, is not dependent on complex and uncertain baryonic processes. Therefore, directly measuring the number and density profile of dark-matter haloes at low masses (below $10^8 M_\odot$) can robustly discriminate between dark-matter models.

[1]Max Planck Institute for Astrophysics, Garching bei München, Germany. [2]Kapteyn Astronomical Institute, University of Groningen, Groningen, The Netherlands. [3]South African Radio Astronomy Observatory, Krugersdorp, South Africa. [4]Department of Physics, University of Pretoria, Pretoria, South Africa. [5]Istituto di Radioastronomia, INAF, Bologna, Italy. [6]Osservatorio di Astrofisica e Scienza dello Spazio, INAF, Bologna, Italy. [7]Dipartimento di Fisica e Astronomia, Alma Mater Studiorum Università di Bologna, Bologna, Italy. [8]Sezione di Bologna, INFN, Bologna, Italy. [9]Department of Physics and Astronomy, University of California Davis, Davis, CA, USA. ✉e-mail: svegetti@mpa-garching.mpg.de

https://doi.org/10.1038/s41550-025-02746-w

Table 1 | Summary statistics for models of detection $\mathcal{V}$ that are the same redshift as the main lens

Model	$\Delta\ln\mathcal{E}$	M ($10^6 M_\odot$)	M_{PM} ($10^5 M_\odot$)	$M_{cyl,90}$ ($10^6 M_\odot$)	R_{ch} (pc)	
UD+PM	0	1.76 ± 0.10	4.25 ± 0.21	1.167 ± 0.039	98 ± 3	$n \to 0$
SER+PM	−3.5	1.79 ± 0.11	4.24 ± 0.20	1.175 ± 0.038	98 ± 3	n = 0.071 ± 0.046
bPL+PM	−11	1.84 ± 0.12	3.70 ± 0.33	1.155 ± 0.043	142 ± 5	t_1 = 0.41 ± 0.08
						t_2 = 14 ± 3
PLU+PM	−17	2.63 ± 0.25	3.80 ± 0.26	1.178 ± 0.043	136 ± 10	–
bPL	−27	2.12 ± 0.14	–	1.164 ± 0.039	193 ± 20	t_1 = 1.29 ± 0.04
						t_2 = 14 ± 4
PJ+PM	−30	3.42 ± 0.43	1.93 ± 0.36	1.164 ± 0.033	266 ± 48	–
NFW+PM	−31	0.97 ± 0.17	3.03 ± 0.32	1.168 ± 0.037	145 ± 30	$\log c_V$ = 5.36 ± 0.20
PL	−38	–	–	1.182 ± 0.033	–	γ = 2.330 ± 0.032
SER	−39	4.54 ± 0.67	–	1.197 ± 0.035	323 ± 84	n = 7.39 ± 0.72
PJ	−39	2.85 ± 0.27	–	1.228 ± 0.040	151 ± 19	–
PL+PM	−39	–	1.83 ± 0.42	1.169 ± 0.032	–	γ = 2.155 ± 0.060
ePL+PM	−40	-	1.81 ± 0.42	1.190 ± 0.034	–	γ = 2.155 ± 0.056
						θ = 95 ± 11°
						q = 0.58 ± 0.13
NFW	−44	0.36 ± 0.03	–	1.197 ± 0.045	24 ± 4	$\log c_V$ = 7.25 ± 0.17
KG_∞	−52	0.43 ± 0.04	–	1.165 ± 0.049	9.24 ± 1.18	–
KG	−53	3.05 ± 0.57	–	1.165 ± 0.050	9.39 ± 1.21	$r_t = (2.47 \pm 2.24) \times 10^4$ pc
KG_{td}	−122	0.87 ± 0.04	–	0.871 ± 0.037	10 ± 5	r_t = 40.89 ± 0.58 pc
PM	−128	1.45 ± 0.07	–	–	–	–
NFW_{CDM}	−147	0.81 ± 0.03	–	1.182 ± 0.042	85 ± 6	$\log c_V$ = 5.96 ± 0.07

Inferred parameters of the mass profile models tested for detection $\mathcal{V}$ that are at the same redshift as the main lens, z=0.881. $\Delta\ln\mathcal{E}$ is the Bayes factor relative to the model that fits the best over all those considered. This model is preferred over a model with no perturber by $\Delta\ln\mathcal{E}_s = 388$. Models are listed in order of decreasing $\Delta\ln\mathcal{E}$. Here, M is the mass of the extended component within r_{max} for all NFW models and for the KG_∞ model, and its total mass M_t for all other models. The characteristic radius R_{ch} is the effective radius of the extended component for all Sérsic models and for the uniform disk with a point mass (UD+PM) and the Plummer with a point mass (PLU+PM) models, the truncation radius for all the pseudo-Jaffe (PJ) models, the core radius for all the King models, r_{max} for all NFW models and the break radius for the broken power law (bPL) models. $M_{cyl,90}$ is the cylindrical mass within a radius of 90 pc. M_{PM} is the total mass of the point-mass component in composite models.

These objects are expected to be dark matter dominated, and most should be completely dark. They can thus only be studied with a gravitational probe, such as strong gravitational lensing.

The JVAS B1938+666 system comprises a massive elliptical galaxy at redshift z_{lens} = 0.881 that gravitationally lenses a powerful radio source at redshift z_{src} = 2.059 (refs. 12–16). At near-infrared wavelengths (2.1 µm, observed frame), the host galaxy of the radio source forms an almost complete Einstein ring[13,15], against which, a $(1.9 \pm 0.1) \times 10^8 M_\odot$ dark object (where $M_\odot$ is the mass of the Sun) has been detected via its gravitational lensing effect[17]. The radio source was observed with the global Very Long Baseline Interferometry (VLBI) network at 1.7 GHz (observed frame), revealing a spectacular and very thin gravitational arc extending over about 200 mas with a width of at most a few milliarcseconds[18]. This arc is clearly separated on the sky from the infrared Einstein ring, and a gravitational imaging analysis of the 1.7-GHz visibility data by Powell et al.[19] detected (at 26σ) the gravitational effects of a second perturber (detection $\mathcal{V}$) that has no obvious luminous counterpart in near-infrared W. M. Keck Telescope adaptive optics data. Powell et al.[19] estimated a mass of $\approx 10^6 M_\odot$ for this object under the assumptions that it lies within the lens galaxy and that its mass profile is well described by a truncated singular isothermal sphere. For clarity, we note that 'gravitational imaging' refers to the lens modelling technique in which low-mass haloes are 'imaged' as regularized pixellated corrections to the otherwise smooth lensing potential. This concept was first introduced by Koopmans[20]. The term is sometimes erroneously used to describe detections obtained with methods that assume a parametrized model for the perturber mass distribution.

We apply the lens modelling code PRONTO[21–26], extended to allow the analysis of high-angular resolution interferometric data, to investigate the likely nature of detection $\mathcal{V}$. We test and compare a wide variety of different parametric models for its mass density profile and redshift using the logarithmic Bayesian evidence ($\ln\mathcal{E}$, that is, the natural logarithm of the probability of a model given the data). These models are chosen to span the most likely candidates for the nature of this unprecedentedly low-mass object: a compact nucleus or black hole, described by a point mass; a globular cluster, described by a King or Plummer profile; a dark-matter halo or sub-halo, described by a conventional Navarro–Frenk–White profile, a truncated singular isothermal profile or a broken power-law profile; and an ultra-compact dwarf galaxy, described by a Sérsic profile. We consider both uninformative priors for the parameters and priors based on observed systems. We also consider composite models that superpose an unresolved central component (a black hole or compact nucleus) on an extended component. We also compare models with the perturber within the lens (at a redshift of 0.881) with models where it is at an unknown redshift along the line of sight.

In total, we tested 23 different models (Tables 1 and 2 and Methods). The best-fitting model (Fig. 1 and Extended Data Table 1) is an object at the main lens redshift made up of a point mass and a uniform, face-on disc (or the equivalent limits of the Sérsic and broken power-law profiles). We designate this as our reference model and give the evidence for other models as $\Delta\ln\mathcal{E}$ relative to it. However, we note that this model has a sharp surface density cut-off at the boundary (139 pc), which is challenging to reconcile with the profiles of known

https://doi.org/10.1038/s41550-025-02746-w

Table 2 | Summary statistics for models of detection $\mathcal{V}$ where the redshift is a free parameter

Model	$\Delta\ln\mathcal{E}$	M_{vir} ($10^6 M_\odot$)	M_{PM} ($10^5 M_\odot$)	$M_{cyl,90}$ ($10^6 M_\odot$)		z
NFW_{field}+PM	−34	5.63 ± 0.75	3.12 ± 0.35	1.209 ± 0.051	$\log c_{vir}$ = 1.68 ± 0.08	0.925 ± 0.059
PL_{field}	−40	–	–	1.632 ± 0.211	γ = 2.405 ± 0.043	1.32 ± 0.16
NFW_{field}	−40	2.86 ± 0.21	–	1.516 ± 0.086	$\log c_{vir}$ = 2.91 ± 0.09	1.469 ± 0.046
PL_{field}+PM	−41	–	1.82 ± 0.45	1.241 ± 0.089	γ = 2.202 ± 0.055	0.983 ± 0.084
$NFW_{CDM,field}$	−75	4.04 ± 0.27	–	1.226 ± 0.039	$\log c_{vir}$ = 2.18 ± 0.04	0.883 ± 0.028

$\Delta\ln\mathcal{E}$ is the Bayes factor relative to the model that fits best over all those considered, that is, the UD+PM in Table 1.

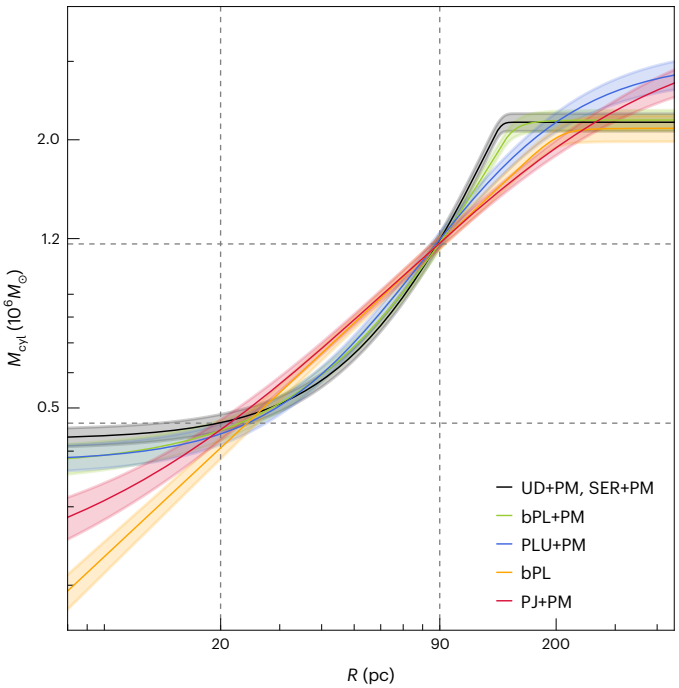

Fig. 1 | The cylindrical mass profile (M_{cyl}) for the six best-fitting models at $z = z_{lens}$. The vertical lines represent the 20 and 90 pc radii, which is also where the different models most closely agree with each other. The horizontal lines are the corresponding values of M_{cyl} for the uniform disk and point mass (UD+PM) model. In the legend, models appear in order of decreasing Bayes factor. Note that the top two models, that is, a uniform disk with a point mass and a Sérsic profile with a point mass (denoted by UD+PM and SER+PM, respectively), are plotted as a single curve and uncertainty band since the differences between them are too small to be easily distinguished at this plotting scale. Also shown are the cylindrical mass profiles for a broken power law with a point mass (bPL+PM), a Plummer sphere with a point mass (PLU+PM), a broken power law (bPL) and a pseudo-Jaffe with a point mass (PJ+PM). The uncertainty bands represent the 1σ confidence interval around the mean.

astrophysical systems. This may reflect some inadequacy of our main lens model at these small scales, or some un-modelled line-of-sight effect that modifies the surface brightness of the radio arc on scales larger than the low-mass perturber. The best astrophysically plausible model we have found for the extended component is a Plummer sphere, but this is already disfavoured by $\Delta\ln\mathcal{E} = -17$. A model with no perturber has $\Delta\ln\mathcal{E} = -388$, corresponding to 28$\sigma$ for Gaussian statistics.

Adopting a single-point-mass model for the perturber leads to a total mass of $M_t = (1.450 \pm 0.066) \times 10^6 M_\odot$, but the data strongly disfavour this model with $\Delta\ln\mathcal{E} = -128$. Hence, our lensing analysis rules out a black hole or unresolved 'point' mass interpretation at high statistical significance. The number density of globular clusters around the Einstein radius of elliptical galaxies is, in some cases, comparable to that of dark-matter sub-haloes (Supplementary Information). Depending on the adopted prior on cluster parameters, the VLBI data disfavour a King model with a $\Delta\ln\mathcal{E}$ between −52 and −122. The best-fitting King profile with a finite truncation radius has a mass of $(3.05 \pm 0.57) \times 10^6 M_\odot$, a core radius of $r_c = 9.39 \pm 1.21$ pc and a tidal radius of $r_t = 24.7 \pm 22.4$ kpc. These properties are extreme compared with known globular clusters, but not outside the observed range (Extended Data Fig. 1). Given the values of the Bayesian evidence, we conclude that the detected object is very unlikely to be a globular cluster in the main lens.

On the other hand, the best-fitting single-component NFW profiles[27] both for a field halo (at $z = 1.469$) and for a sub-halo in the lens are highly concentrated, with $\log c_{vir} = \log(r_{vir}/r_s) = 2.91 \pm 0.09$ and $\log c_v = \log(2 \times (V_{max}/(H_z r_{max}))^2) = 7.25 \pm 0.17$, respectively. For comparison, the expected concentrations at these masses and redshifts in a ΛCDM cosmology are $\log c_{vir} = 1.10 \pm 0.15$ (ref. 28) and $\log c_v = 3.90 \pm 0.02$ (ref. 29). Hence, we find a discrepancy at the 10σ to 20σ level between our observations and theoretical expectations. Imposing such a ΛCDM prior leads to a dramatic drop in Bayesian evidence of −75 and −147 for the field halo and sub-halo cases, respectively (see Extended Data Fig. 2 for a comparison of the measured and predicted maximum radius and velocity). Adding a central point mass reduces the tension between the inferred NFW parameters and the ΛCDM expectation to 3σ and 6σ, but this has little meaning since adding a point mass of the mass we infer would substantially modify the central profile of the host halo. Even with the NFW parameters and the central point mass left free, all NFW models for the extended component are strongly excluded by the data, with the best model of this family (for which the mass of the compact object is $0.3 \times M_{max}$) having $\Delta\ln\mathcal{E} = -31$ relative to our best-fit model.

In our analysis, detection $\mathcal{V}$ is best explained by a uniform-surface-density, face-on disk of outer radius $R = 139 \pm 4$ pc centred on an unresolved component containing 19% of the total mass, $(1.8 \pm 0.1) \times 10^6 M_\odot$. The central object could potentially be a black hole or a nuclear star cluster. In CDM and WDM, the formation of a black hole at the centre of galaxies is the result of complex and uncertain baryonic processes. In the mass regime of detection $\mathcal{V}$, haloes are expected to have no stars and to be well described by a single NFW profile. A fully dark halo with properties consistent with our best-fit model thus seems extremely implausible in CDM and WDM models (see Supplementary Information for more details). However, for suitably chosen cross-sections, it may be achievable in SIDM models, where gravo-thermal evolution and core collapse can lead to the formation of black holes at the centre of dark-matter haloes (see, for example, refs. 7,11,30). Reproducing the VLBI data would require a halo that had a CDM equivalent with a maximum circular velocity of $v_{max} \approx 5$ km s^{-1} and that is deep in the core collapse regime by the observed redshift of 0.881, implying a velocity averaged interaction cross-section of ≈ 800 cm^2 g^{-1}, or more (Extended Data Fig. 3 and Supplementary Information).

Alternatively, the lensing signature of detection $\mathcal{V}$ could be that of an ultracompact galaxy with a central massive black hole or nuclear star cluster. These are a distinct class of small, dense stellar systems with masses lying between those of globular clusters and those of normal dwarf galaxies. First discovered in nearby galaxy clusters such as Fornax and Virgo (see, for example, ref. 31), they are some of the densest galaxies currently known. Ultracompact galaxies are thought to form in a variety of ways, for example, by tidal stripping of dwarf galaxies in dense environments. Our best-fit model has an overall size

and mass consistent with those of known ultracompact galaxies and local nuclear star clusters (Extended Data Fig. 1 and Supplementary Information), although their radial light distributions are markedly more centrally concentrated than the uniform mass surface density favoured here.

This is the third object to be individually 'gravitationally imaged' to date[17,32]. All three detections have properties which, at different statistical levels, appear unusual when compared with dark-matter-dominated haloes in the CDM and WDM paradigms[33–36]. Our analysis (see Supplementary Information for more details), together with those of previous detections, suggests that, if deeper observations confirm that these objects are dark matter dominated rather than star dominated, as ultracompact galaxies and nuclear star clusters are, then dark matter cannot be collisionless. Hence, our results could have important implications for the nature of dark matter and the standard cosmological model. However, more numerical and theoretical work is needed to obtain robust predictions from SIDM models at the spatial scales and evolutionary phases relevant to the VLBI data, and to verify that all three detections are consistently explained by the same parameters for the SIDM cross-section.

Methods

Data

The data for the radio source JVAS B1938+666 used in this analysis were taken with a global VLBI array consisting of the European VLBI Network (EVN, 11 antennas), the Very Long Baseline Array (VLBA, 10 antennas) and the Green Bank Telescope, at a central observing frequency of 1.7 GHz and with a bandwidth of 64 MHz (ref. 18). This observational set-up resulted in an angular resolution (the so-called beam size) of 7.4 mas × 4.7 mas, for a natural weighting of the visibilities. The observation lasted 14 h with a data recording rate of 512 Mbits s^{-1} (ID GM068, principal investigator McKean).

Using these data, an extended but extremely thin gravitational arc was found[18], superposed on which a low-mass object was discovered by Powell et al.[19]. Here, we focus on the properties of this new object (detection $\mathcal{V}$) and consider possible explanations for its nature in the context of known astrophysical objects and various dark-matter models.

Lens model

We use the Bayesian lens modelling code PRONTO[21–26], which fits the data directly in visibility space. The background unlensed source is reconstructed in a pixellated, regularized fashion on a Delaunay tessellation with a magnification-adaptive resolution. The sum of the following components gives the mass density profile of the macro-model: an elliptical power law for the main lens galaxy, multipoles of order $m = 3$ and $m = 4$ (as defined in ref. 37) and an external shear component of strength Γ and position angle Γ_θ. We also include the contribution of a $\approx 10^8 M_\odot$ low-mass halo, first detected in ref. 17 in the same gravitational lens system (in the following, referred to as detection $\mathcal{A}$). Powell et al.[19] have shown that, while the VLBI data do not provide a strong constraint on the redshift of detection $\mathcal{A}$, they strongly disfavour the $z = 1.4$ value proposed in ref. 38. Recently, Tajalli et al.[36] presented a re-analysis of the W. M. Keck Telescope adaptive optics (Keck AO hereafter) data for JVAS B1938+666, showing that detection $\mathcal{A}$ is indeed a field halo, but at much lower redshift, $z = 0.13 \pm 0.07$. We note that the Keck AO data, when compared with the VLBI data analysed here, are significantly more sensitive to the presence and properties of detection $\mathcal{A}$, as it falls right on top of the lensed (rest-frame) optical emission, while offset relative to the 1.7-GHz arc. In fact, it was demonstrated in ref. 19 that assumptions about detection $\mathcal{A}$ do not affect the detection and the inferred properties of the object under study here (which we refer to as detection $\mathcal{V}$). Hence, for simplicity, we include detection $\mathcal{A}$ as a pseudo-Jaffe sub-halo at the lens redshift.

The dimensionless surface mass density (that is, the convergence) profile for an elliptical power law of axis ratio q and three-dimensional (3D) slope γ (with $\gamma = 2$ representing an isothermal profile) is given by

$$\kappa(R) = \kappa_0 \left(1 - \frac{\gamma}{4}\right) \frac{q^{\gamma-3/2}}{(R/r_\mathrm{p})^{(\gamma-1)}}, \tag{1}$$

with radius $R = \sqrt{q^2(r_\mathrm{c}^2 + x^2) + y^2}$ and normalization κ_0. We calculate the corresponding deflection angle using FASTELL[39]. With the exception of the core radius ($r_\mathrm{c} \equiv 10^{-4}$ arcsec), the pivot radius ($r_\mathrm{p} \equiv 1$ arcsec) and the redshift of detection $\mathcal{A}$ ($z_\mathcal{A} \equiv z_\mathrm{lens}$), all other parameters of the macro-model are left free to vary (for a total of 16 free parameters including the strength of the source regularization).

We model detection $\mathcal{V}$ with the following circularly symmetric profiles: a single power law (PL), a broken power law (bPL), a truncated singular isothermal or pseudo-Jaffe (PJ) profile, a Navarro–Frenk–White (NFW) profile, a King model (KG), a Sérsic (SER) profile, a Plummer (PLU) profile and a point mass (PM). We also tested an elliptical power law (ePL) profile and a number of composite models that add a central point mass to one of the above models for the extended component. In all cases, we keep the position on the sky free.

The convergence of the PL model follows equation (1) with $q = 1$. Free parameters of the model are the normalization κ_0 and the slope γ. For the core radius, we choose a very small value that is well below the resolution of the data. We consider both a sub-halo model (PL) where the redshift is fixed to that of the main deflector and a field halo model ($\mathrm{PL_{field}}$) where the redshift is a free parameter.

For the broken power law model, we adopt the representation of ref. 40 for the convergence

$$\kappa(x) = \begin{cases} \kappa_\mathrm{b}\, x^{-t_1} & \text{for } x \le 1 \\ \kappa_\mathrm{b}\, x^{-t_2} & \text{for } x > 1 \end{cases}, \tag{2}$$

where $x = R/r_\mathrm{b}$. The break radius r_b, the inner and outer logarithmic slopes t_1 and t_2, and the normalization at the break radius κ_b are all adjustable parameters.

The PJ profile is described as follows:[41]

$$\kappa(x) = \kappa_0 \left(\frac{1}{x} - \frac{1}{\sqrt{1+x^2}}\right), \tag{3}$$

with $x = R/r_\mathrm{t}$. This model has two degrees of freedom, that is, the total mass $M_\mathrm{t} = 2\pi r_\mathrm{t}^2 \kappa_0 \Sigma_\mathrm{c}$ and the truncation radius r_t, where Σ_c is the critical surface mass density.

The convergence of the NFW[27] profile is given by

$$\kappa(x) = 2\kappa_\mathrm{s} \frac{1 - F(x)}{x^2 - 1}, \tag{4}$$

with $x = R/r_\mathrm{s}$, $\kappa_\mathrm{s} = \rho_\mathrm{s} r_\mathrm{s} \Sigma_\mathrm{c}^{-1}$ and

$$F(x) = \begin{cases} \frac{1}{\sqrt{x^2-1}} \tan^{-1}\sqrt{x^2-1} & \text{for } x > 1 \\ \frac{1}{\sqrt{1-x^2}} \tanh^{-1}\sqrt{1-x^2} & \text{for } x < 1 \\ 1 & \text{for } x = 1 \end{cases}. \tag{5}$$

Here, the density ρ_s and the surface mass density κ_s are taken at the scale radius r_s. We consider two cases: one in which the object is a sub-halo within the lens galaxy (NFW) and one in which its redshift can vary between the observer and the source ($\mathrm{NFW_{field}}$). For sub-haloes, we characterize the profile by the peak circular velocity radius r_max and M_max, the corresponding enclosed mass in 3D; further, we compare with N-body simulations using the concentration $c_\mathrm{v} = 2 \times (V_\mathrm{max}/(H_z r_\mathrm{max}))^2$, where V_max is the peak circular velocity and H_z is the Hubble constant at redshift z. For field haloes, we use the more conventional parameter pair: the virial mass M_vir and the concentration

$c_{vir} = r_{vir}/r_s$. For both the PL_{field} and the NFW_{field} models, the prior on the redshift is set to be uniform in the comoving distance of the perturber.

The King model is used to represent globular cluster (GC) profiles. Its convergence is given by the expression

$$\kappa(x) = \kappa_0 \left[\frac{1}{\sqrt{1+x^2}} - \frac{1}{\sqrt{1+t^2}} \right], \quad (6)$$

where $x = R/r_c$ and $t = r_t/r_c$. The degrees of freedom in this case are the core radius r_c, the truncation (or 'tidal') radius r_t and the total mass. The latter is given by $M_t = \pi\kappa_0 r_c^2 \Sigma_c f(t)$, with

$$f(t) = \log(1+t^2) + \frac{t^2 - 4\sqrt{1+t^2}\left(\sqrt{1+t^2}-1\right)}{1+t^2}. \quad (7)$$

We consider three cases. In the first, the truncation radius r_t is taken to be equivalent to the tidal radius, estimated using the expression[42]

$$r_t = \frac{2}{3}\left(\frac{M_t}{2M_{lens}(<d)}\right)^{1/3} d. \quad (8)$$

Here, d is the projected distance of the detected object from the centre of the lens galaxy and $M_{lens}(<d)$ is the mass of the main deflector within a sphere of radius d. We refer to this model as KG_{td} and set the prior on the concentration $c = \log r_t/r_c$ to be uniform between 0.3 and 2.7, in line with typical values for GCs in the Local Universe[43]. For the second case (KG), we leave the total mass, the core radius and $t^{-1} = r_c/r_t$ free to vary, with the prior on the latter being uniform between 10^{-4} and 0.5 to encompass all known values for GCs and ultra-compact dwarf galaxies (UCDs; see below for more details). For the third version of the King profile (KG_∞) we allow $r_t \to \infty$. As the total mass of this profile is not finite, we define as free parameters the mass M_{max} within the peak circular velocity radius $r_{max} \approx 2.919 \times r_c$ and the core radius itself, r_c.

The majority of UCDs have been shown to be well described by a multi-component King or Sérsic profiles (see, for example, ref. 44). The convergence profile of the latter is given by

$$\kappa(x) = \kappa_e \exp\left[-b_n(x^{1/n} - 1)\right], \quad (9)$$

with $x = R/R_e$ and K_e as the convergence at the effective radius. There are three degrees of freedom: the effective radius R_e, the index n and the total mass $M_t = 2\pi R_e^2 \kappa_e \Sigma_c n \exp(b_n)/b_n^{2n}\,\Gamma[2n]$. Here, $\Gamma[2n]$ is the complete gamma function. The constant b_n is set by the requirement that half the total mass be projected within R_e. In the limit $n \to 0$

$$\kappa(x) = \begin{cases} \frac{M_t}{2}x^2 & \text{for } x < \sqrt{2} \\ M_t & \text{for } x \geq \sqrt{2} \end{cases}. \quad (10)$$

Hence, in this case, the Sérsic profile has a constant surface mass density and a finite size, and we refer to it as a uniform disk (UD). This model has only two degrees of freedom: the total mass and the effective radius. It is also a limiting case of the bPL model for $t_1 = 0$ and $t_2 \to \infty$.

The Plummer profile (PLU) was initially introduced to describe the light distribution of globular clusters[45] and is now often used as an example of a simple, fully analytic model for spherical stellar systems. We consider it because, with an additional central point mass, it turns out to be a relatively good description of our data. The convergence of the Plummer model is given by

$$\kappa(x) = \frac{\kappa_0}{(1+x^2)^2}, \quad (11)$$

with $x = r/r_s$. We take the free parameters of this model to be the total mass M_t and the scale radius r_s.

Model ranking

Tables 1 and 2 list the mean and 1σ uncertainty on the inferred parameters for all the different profiles that we tested. When the perturbers are located at a higher redshift than the main lens, we quote their position on the latter plane. Regardless of the assumed mass density profile, the object is detected at high statistical significance, with a Bayes factor relative to a model with no perturber of $241 \leq \Delta \ln \mathcal{E}_s \leq 388$, corresponding to a detection significance between 22σ and 28σ assuming Gaussian statistics.

The best-fitting model is the UD+PM model. In the following, the Bayes factor of a given model $\mathcal{M}$ is measured, unless otherwise specified, relative to this best model, that is, $\Delta \ln \mathcal{E} = \ln \mathcal{E}_{\mathcal{M}} - \ln \mathcal{E}_{UP+PM}$. Extended Data Table 1 reports the inferred parameters for the macro-model (including detection $\mathcal{A}$). We only quote these parameters for the best model (UD +PM), but we find that they change very little for different models for the profile of detection $\mathcal{V}$. Images of the system at a variety of scales, showing the position of detections $\mathcal{A}$ and $\mathcal{V}$ relative to the lensed source emission in the radio and the near-infrared, can be found in fig. 1 of ref. 19.

For models that do not include the PM component, we find small differences in the Bayes factor (at most 4) between those with the perturber at the redshift of the lens and those where its redshift is free. The latter converge to $z \approx 1.4$ and are characterized by steeper slopes for the PL models and higher concentrations for the NFW profiles. This is related to the degeneracy between these quantities and redshift, whereby objects located along the line-of-sight need to be more massive and to have steeper or more concentrated profiles to provide the most similar lensing effect to an object within the lens (Tajalli et al. in prep.). Once a PM component is included, the field models converge to a redshift consistent with that of the main lens, and their Bayes factor increases considerably. This indicates that detection $\mathcal{V}$ is very likely within the main deflector. In the following, we therefore focus primarily on sub-halo models with $z \equiv z_{lens}$.

The top model UD+PM is followed closely by SER+PM ($\Delta \ln \mathcal{E} = -3.5$) and bPL+PM ($\Delta \ln \mathcal{E} = -11$). This is not surprising, since the parameters found for these two models are close to the limits where their mass profiles become identical to that of UD+PM. However, all three models are bounded by an implausibly steep surface mass density cut-off. The fourth best model is PLU+PM ($\Delta \ln \mathcal{E} = -17$). This result is also unsurprising since equation (11) shows the convergence of this profile to be almost constant out to the scale radius, where it cuts off steeply. Sub-halo models with a point mass and an extended profile more similar to those usually assumed for dark-matter haloes or real stellar systems are significantly disfavoured relative to these top models, with Bayes factors ranging from $\Delta \ln \mathcal{E} = -30$ for PJ+PM to $\Delta \ln \mathcal{E} = -40$ for ePL+PM. The best model without a central point mass is bPL with $\Delta \ln \mathcal{E} = -27$, followed by PL, SER, PJ and NFW in that order, with the last having a high concentration and $\Delta \ln \mathcal{E} = -44$; when a ΛCDM concentration prior is adopted, this drops catastrophically to $\Delta \ln \mathcal{E} = -147$. All versions of the King profile are strongly disfavoured, with Bayes factors ranging from −52 for KG_∞ to −122 for KG_{td}. A point mass is also very strongly excluded with $\Delta \ln \mathcal{E} = -128$. Hence, from the lens modelling alone, we conclude that the data exclude a naked black hole or a compact system with a radius less than 10 or 20 pc. In the Supplementary Information, we discuss how these profile properties compare with predictions from different dark-matter models and to the observed properties of GCs and UCDs.

Strong gravitational lensing is known to provide a robust and model-independent measure of the projected mass within an appropriately chosen radius. However, our results show that, in the system we consider here, the projected mass profile is tightly constrained over a broad range of radii. This is a consequence of the fact that, for low-mass perturbers, the angular size of the source is larger than that of the deflector, so that the observed image structure constrains the enclosed mass over a range of radii. In the specific case of detection $\mathcal{V}$,

we find that all models that provide a decent fit to the data agree in the values they predict for the enclosed (cylindrical) mass, M_{cyl}, both at 20 pc and (most tightly) at 90 pc. This applies to perturbers both within and along the line of sight to the main lens. Indeed, of the 12 models with $\Delta \log \mathcal{E} > -40$, 10 give a best value of $M_{cyl,90}$ that differs by less than 3% from that of the best model, while for $M_{cyl,20}$, 10 models differ from the best model by less than 8%.

Models such as KG_{td} and PM that do not lead to the correct mass at either radius, or the NFW_{CDM} model, which fails to match at 20 pc, are strongly disfavoured. Leaving aside these models, the ranking of the other profiles depends both on the curvature of the M_{cyl} profile between 20 and 90 pc and on the rapidity with which the mass increases at larger radii. Thus, the gradient of the UD+PM and PLU+PM models is increasing outwards, while for the models with $-27 > \Delta \log \mathcal{E} > -32$, it is constant over this range, and for most of the less favoured models it is decreasing outwards (Fig. 1 and Supplementary Fig. 1). We demonstrate explicitly that the data also constrain the profile beyond 90 pc by running a bPL+PM model for which the inner point mass, the break radius and the outer slope were left free, but the inner slope was fixed to that of the best PL+PM model. We found this model to predict an essentially identical $M_{cyl}(R)$ to PL+PM within the break radius, 98 pc, but a markedly steeper profile at larger radii ($t_2 = 1.96$ as compared with $t_1 = 1.155$). The $\Delta \log \mathcal{E}$ for this extra model was −32, a full 7 units better than the PL+PM model, indicating that a reduced mass beyond 100 pc is strongly preferred by the data. Presumably, this reflects the fact that the lensed arc extends well beyond this distance, and its surface brightness distribution provides extra constraining power.

Irrespective of the choice of model, the position of the perturber on the plane of the lens is extremely well constrained, with an average error of $\sigma_x = 0.1$ mas and $\sigma_y = 0.2$ mas (equivalent to 0.8–1.6 pc in the plane of the lens). The error on the x coordinate is smaller by a factor of 2 because of the corresponding smaller size of the lensed arc in the x direction, a result of the strong tangential magnification experienced by the background source, together with the location of the critical curves; any small shift of the perturber along x corresponds to a substantial change in its gravitational effect. The position is also consistent among the different models, with a standard deviation of 1.1 and 1.5 mas along the x and y axis, respectively. The largest shift relative to our best model is displayed by the PM model, with $|\Delta x| = 5$ mas and $|\Delta y| = 4$ mas. This is related to the fact that the PM is the most centrally concentrated profile we consider and, so, has the largest capability to perturb the lensed images. If located closer to the arc, a PM would further split the arc into further multiple images, but there is no evidence for this in the observational data.

Supplementary Fig. 1 compares the $M_{cyl}(R)$ curves for all our profile models, while Supplementary Figs. 2–24 display the full posterior distributions for their parameters.

Data availability

The dataset is publicly available via the EVN archive at https://archive.jive.nl/scripts/portal.php (observation ID GM068, principal investigator McKean).

Code availability

The modelling code PRONTO is not publicly available. The reader interested in using this code can contact svegetti@mpa-garching.mpg.de. The methodology used for the lens modelling is fully explained by Powell et al.[25].

References

1. Springel, V. et al. The Aquarius Project: the subhaloes of galactic haloes. *Mon. Not. R. Astron. Soc.* **391**, 1685–1711 (2008).
2. Lovell, M. R. et al. The haloes of bright satellite galaxies in a warm dark matter universe. *Mon. Not. R. Astron. Soc.* **420**, 2318–2324 (2012).
3. Lovell, M. R. The halo mass function in alternative dark matter models. *Mon. Not. R. Astron. Soc.* **493**, 11–15 (2020).
4. Kahlhoefer, F., Kaplinghat, M., Slatyer, T. R. & Wu, C.-L. Diversity in density profiles of self-interacting dark matter satellite halos. *J. Cosmol. Astropart. Phys.* **2019**, 010–023 (2019).
5. Zavala, J., Lovell, M. R., Vogelsberger, M. & Burger, J. D. Diverse dark matter density at sub-kiloparsec scales in Milky Way satellites: Implications for the nature of dark matter. *Phys. Rev. D* **100**, 063007 (2019).
6. Nishikawa, H., Boddy, K. K. & Kaplinghat, M. Accelerated core collapse in tidally stripped self-interacting dark matter halos. *Phys. Rev. D* **101**, 063009 (2020).
7. Turner, H. C., Lovell, M. R., Zavala, J. & Vogelsberger, M. The onset of gravothermal core collapse in velocity-dependent self-interacting dark matter subhaloes. *Mon. Not. R. Astron. Soc.* **505**, 5327–5339 (2021).
8. Zeng, Z. C. et al. Core-collapse, evaporation, and tidal effects: the life story of a self-interacting dark matter subhalo. *Mon. Not. R. Astron. Soc.* **513**, 4845–4868 (2022).
9. Lynden-Bell, D. & Wood, R. The gravo-thermal catastrophe in isothermal spheres and the onset of red-giant structure for stellar systems. *Mon. Not. R. Astron. Soc.* **138**, 495–525 (1968).
10. Balberg, S., Shapiro, S. L. & Inagaki, S. Self-interacting dark matter halos and the gravothermal catastrophe. *Astrophys. J.* **568**, 475–487 (2002).
11. Outmezguine, N. J., Boddy, K. K., Gad-Nasr, S., Kaplinghat, M. & Sagunski, L. Universal gravothermal evolution of isolated self-interacting dark matter halos for velocity-dependent cross-sections. *Mon. Not. R. Astron. Soc.* **523**, 4786–4800 (2023).
12. King, L. J. et al. Multifrequency radio observations of the gravitational lens system B1938+666. *Mon. Not. R. Astron. Soc.* **289**, 450–456 (1997).
13. King, L. J. et al. A complete infrared Einstein ring in the gravitational lens system B1938+666. *Mon. Not. R. Astron. Soc.* **295**, 41–44 (1998).
14. Riechers, D. A. Molecular gas in lensed $z>2$ quasar host galaxies and the star formation law for galaxies with luminous active galactic nuclei. *Astrophys. J.* **730**, 108–123 (2011).
15. Lagattuta, D. J. et al. SHARP – I. A high-resolution multiband view of the infrared Einstein ring of JVAS B1938+666. *Mon. Not. R. Astron. Soc.* **424**, 2800–2810 (2012).
16. Spingola, C. et al. SHARP - VI. Evidence for CO (1-0) molecular gas extended on kpc-scales in AGN star-forming galaxies at high redshift. *Mon. Not. R. Astron. Soc.* **495**, 2387–2407 (2020).
17. Vegetti, S. et al. Gravitational detection of a low-mass dark satellite galaxy at cosmological distance. *Nature* **481**, 341–343 (2012).
18. McKean, J. P., Spingola, C., Powell, D. M. & Vegetti, S. An extended and extremely thin gravitational arc from a lensed compact symmetric object at redshift 2.059. *Mon. Not. R. Astron. Soc.* **544**, L24–L30 (2025).
19. Powell, D. et al. A million-solar-mass object detected at a cosmological distance using gravitational imaging. *Nat. Astron.* https://doi.org/10.1038/s41550-025-02651-2 (2025)
20. Koopmans, L. V. E. Gravitational imaging of cold dark matter substructures. *Mon. Not. R. Astron. Soc.* **363**, 1136–1144 (2005).
21. Vegetti, S. & Koopmans, L. V. E. Bayesian strong gravitational-lens modelling on adaptive grids: objective detection of mass substructure in galaxies. *Mon. Not. R. Astron. Soc.* **392**, 945–963 (2009).
22. Rybak, M., McKean, J. P., Vegetti, S., Andreani, P. & White, S. D. M. ALMA imaging of SDP.81 – I. A pixelated reconstruction of the far-infrared continuum emission. *Mon. Not. R. Astron. Soc.* **451**, 40–44 (2015).

23. Rizzo, F., Vegetti, S., Fraternali, F. & Di Teodoro, E. A novel 3D technique to study the kinematics of lensed galaxies. *Mon. Not. R. Astron. Soc.* **481**, 5606–5629 (2018).
24. Ritondale, E., Auger, M. W., Vegetti, S. & McKean, J. P. Resolving on 100 pc scales the UV-continuum in Lyman-α emitters between redshift 2 and 3 with gravitational lensing. *Mon. Not. R. Astron. Soc.* **482**, 4744–4762 (2019).
25. Powell, D. et al. A novel approach to visibility-space modelling of interferometric gravitational lens observations at high angular resolution. *Mon. Not. R. Astron. Soc.* **501**, 515–530 (2021).
26. Ndiritu, S., Vegetti, S., Powell, D. M. & McKean, J. P. A self-consistent framework to study magnetic fields with strong gravitational lensing and polarised radio sources. *Mon. Not. R. Astron. Soc.* **538**, 671–697 (2025).
27. Navarro, J. F., Frenk, C. S. & White, S. D. M. The structure of cold dark matter halos. *Astrophys. J.* **462**, 563–585 (1996).
28. Duffy, A. R., Schaye, J., Kay, S. T. & Dalla Vecchia, C. Dark matter halo concentrations in the Wilkinson Microwave Anisotropy Probe year 5 cosmology. *Mon. Not. R. Astron. Soc.* **390**, 64–68 (2008).
29. Moliné, Á. et al. ΛCDM halo substructure properties revealed with high-resolution and large-volume cosmological simulations. *Mon. Not. R. Astron. Soc.* **518**, 157–173 (2023).
30. Yang, D., Nadler, E. O., Yu, H.-B. & Zhong, Y.-M. A parametric model for self-interacting dark matter halos. *J. Cosmol. Astropart. Phys.* **2024**, 032–054 (2024).
31. Hilker, M., Infante, L., Vieira, G., Kissler-Patig, M. & Richtler, T. The central region of the Fornax cluster. II. Spectroscopy and radial velocities of member and background galaxies. *Astron. Astrophys. Suppl.* **134**, 75–86 (1999).
32. Vegetti, S., Koopmans, L. V. E., Bolton, A., Treu, T. & Gavazzi, R. Detection of a dark substructure through gravitational imaging. *Mon. Not. R. Astron. Soc.* **408**, 1969–1981 (2010).
33. Minor, Q., Gad-Nasr, S., Kaplinghat, M. & Vegetti, S. An unexpected high concentration for the dark substructure in the gravitational lens SDSSJ0946+1006. *Mon. Not. R. Astron. Soc.* **507**, 1662–1683 (2021).
34. Despali, G. et al. Detecting low-mass haloes with strong gravitational lensing II: constraints on the density profiles of two detected subhaloes. *Astron. Astrophys.* **699**, A222–A245 (2025).
35. Enzi, W. J. R., Krawczyk, C. M., Ballard, D. J. & Collett, T. E. The overconcentrated dark halo in the strong lens SDSS J0946+1006 is a subhalo: evidence for self interacting dark matter? *Mon. Not. R. Astron. Soc.* **540**, 247–263 (2025).
36. Tajalli, M. et al. SHARP – IX. The dense, low-mass perturbers in B1938+666 and J0946+1006: implications for cold and self-interacting dark matter. *Mon. Not. R. Astron. Soc.* **543**, 540–564 (2025).
37. O'Riordan, C. M. & Vegetti, S. Angular complexity in strong lens substructure detection. *Mon. Not. R. Astron. Soc.* **528**, 1757–1768 (2024).
38. Sengül, A. Ç., Dvorkin, C., Ostdiek, B. & Tsang, A. Substructure detection reanalysed: dark perturber shown to be a line-of-sight halo. *Mon. Not. R. Astron. Soc.* **515**, 4391–4401 (2022).
39. Barkana, R. FASTELL: fast calculation of a family of elliptical mass gravitational lens models. *Astrophysics Source Code Library* https://ascl.net/9910.003 (1999)
40. O'Riordan, C. M., Warren, S. J. & Mortlock, D. J. Galaxy mass profiles from strong lensing – III. The two-dimensional broken power-law model. *Mon. Not. R. Astron. Soc.* **501**, 3687–3694 (2021).
41. Jaffe, W. A simple model for the distribution of light in spherical galaxies. *Mon. Not. R. Astron. Soc.* **202**, 995–999 (1983).
42. Bellazzini, M. Tidal radii of globular clusters and the mass of the Milky Way. *Mon. Not. R. Astron. Soc.* **347**, 119–124 (2004).
43. Harris, W.E. A new catalog of globular clusters in the Milky Way. Preprint at https://arxiv.org/abs/1012.3224 (2010).
44. Wang, K. et al. An evolutionary continuum from nucleated dwarf galaxies to star clusters. *Nature* **623**, 296–300 (2023).
45. Plummer, H. C. On the problem of distribution in globular star clusters. *Mon. Not. R. Astron. Soc.* **71**, 460–470 (1911).
46. Calura, F. et al. Sub-parsec resolution cosmological simulations of star-forming clumps at high redshift with feedback of individual stars. *Mon. Not. R. Astron. Soc.* **516**, 5914–5934 (2022).
47. Baumgardt, H., Hénault-Brunet, V., Dickson, N. & Sollima, A. Evidence for a bottom-light initial mass function in massive star clusters. *Mon. Not. R. Astron. Soc.* **521**, 3991–4008 (2023).
48. Norris, M. A. et al. The AIMSS Project – I. Bridging the star cluster-galaxy divide. *Mon. Not. R. Astron. Soc.* **443**, 1151–1172 (2014).
49. Meštrić, U. et al. Exploring the physical properties of lensed star-forming clumps at $2 \leq z \leq 6$. *Mon. Not. R. Astron. Soc.* **516**, 3532–3555 (2022).
50. Hiroshima, N., Ando, S. & Ishiyama, T. Modelling the evolution of dark matter substructure and annihilation boost. *Phys. Rev. D* **97**, 123002 (2018).
51. Ando, S., Ishiyama, T. & Hiroshima, N. Halo substructure boosts to the signatures of dark matter annihilation. *Galaxies* **7**, 68 (2019).

Acknowledgements

S.V. and D.M. are grateful to L. V. Sales, E. Peng and F. Calura for kindly sharing the data required to reproduce fig. 2 of ref. 44 and fig. 12 of ref. 46, respectively. S.V. thanks A. Zocco for providing clever computational solutions. S.V. thanks H. Yu, D. Yang and S. Ando for insightful discussion on SIDM. This research was carried out on the High-Performance Computing resources of the Raven cluster at the Max Planck Computing and Data Facility (MPCDF) in Garching, operated by the Max Planck Society (MPG). S.V. and D.M.P. have received funding from the European Research Council (ERC) under the European Union's Horizon 2020 research and innovation programme (grant agreement no. 758853). S.V. thanks the Max Planck Society for support through a Max Planck Lise Meitner Group. This work is based on research supported in part by the National Research Foundation of South Africa (grant no. 128943). C.S. acknowledges financial support from INAF under the project 'Collaborative research on VLBI as an ultimate test to ΛCDM model' as part of the Ricerca Fondamentale 2022. This work was supported in part by the Italian Ministry of Foreign Affairs and International Cooperation (grant no. PGRZA23GR03) and by the Italian Ministry of University and Research (grant no. FIS-2023-01611 – CUP C53C25000300001). D.M. acknowledges financial support from PRIN-MIUR-22: 'CHRONOS: adjusting the clock(s) to unveil the CHRONO-chemo-dynamical Structure of the Galaxy' (PI: S. Cassisi). G.D. acknowledges the funding by the European Union – NextGenerationEU, in the framework of the HPC project 'National Centre for HPC, Big Data and Quantum Computing' (PNRR – M4C2 – I1.4 – CN00000013 – CUP J33C22001170001).

Author contributions

S.V. contributed to the development of the lens modelling code and carried out all the analysis presented in the paper. S.D.M.W. derived the fit to the SIDM profiles and contributed extensively to the interpretation of the results. J.P.M. initiated and led the data collection, and contributed to the calibration and imaging. D.M.P. was the main developer of PRONTO and contributed to the smooth modelling of the data. C.S. contributed to this work by calibrating the VLBI data and writing the 'Data'section. D.M. contributed to the interpretation of the results in terms of globular cluster properties. G.D. contributed to the interpretation of the results and discussions on SIDM predictions. C.D.F. contributed to the interpretation of the results and obtained the Keck AO data that were used for the first detection of A.

Funding
Open access funding provided by Max Planck Society.

Competing interests
The authors declare no competing interests.

Additional information
Extended data is available for this paper at https://doi.org/10.1038/s41550-025-02746-w.

Supplementary information The online version contains supplementary material available at https://doi.org/10.1038/s41550-025-02746-w.

Correspondence and requests for materials should be addressed to Simona Vegetti.

Peer review information *Nature Astronomy* thanks the anonymous reviewers for their contribution to the peer review of this work.

https://doi.org/10.1038/s41550-025-02746-w

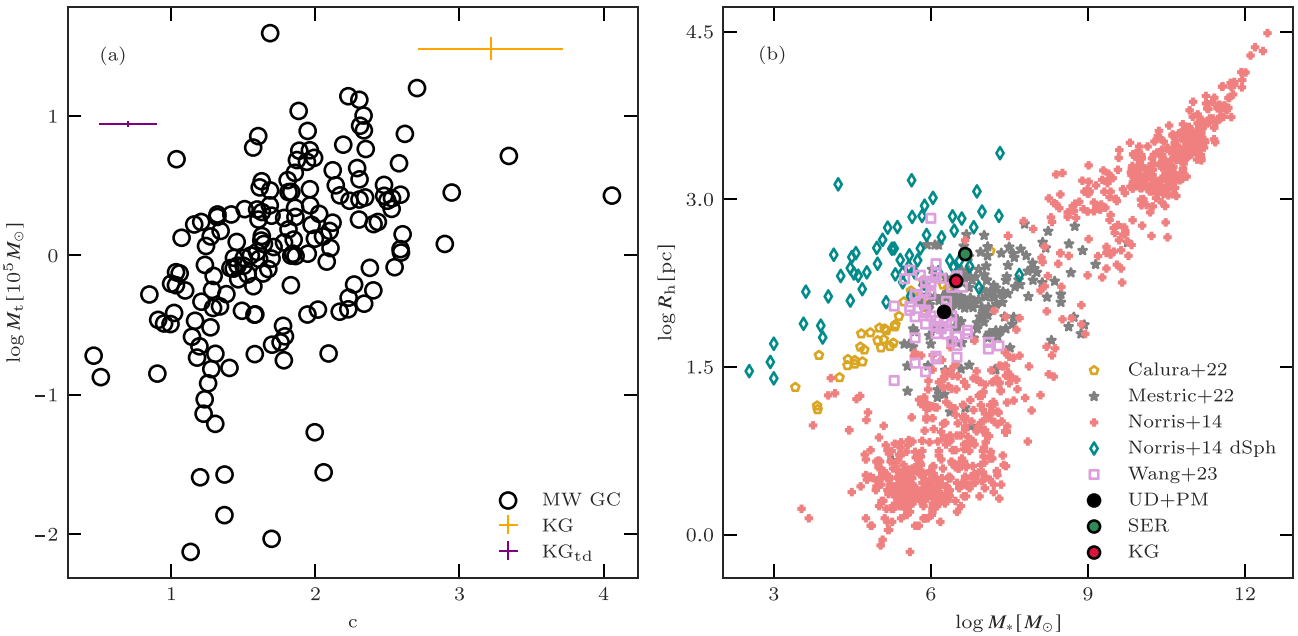

Extended Data Fig. 1 | Comparison with known stellar systems. Panel (**a**): Mass and concentration for the GCs in the Milky Way [black circles,[47]] and for the KG_{td} and KG models of detection $\mathcal{V}$ (coloured points, mean value and 1-σ uncertainty). Panel (**b**): relation between stellar mass and effective radius from observations of different types of objects: dSph galaxies at $z = 0$ [green diamonds,[48]], strongly lensed star-forming clumps at $z = 2$ to 6 [gray stars,[49]], eUCDs in the Virgo cluster [pink squares,[44]], dEs, dS0s, nuclear star clusters, GCs, UCDs, cEs and YMCs at $z = 0$ [coral crosses,[48]]. The yellow diamonds represent simulated star-forming stellar clusters at $z \sim 6$. The green, red and black dots are detection $\mathcal{V}$ when modelled with a Sérsic profile of index $n \sim 7$, a King profile and a Sérsic profile of index $n \to 0$ with a point-mass, respectively.

https://doi.org/10.1038/s41550-025-02746-w

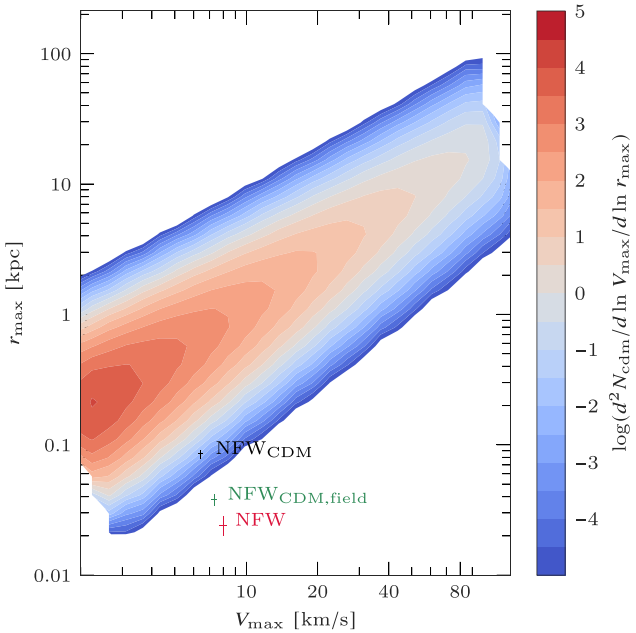

Extended Data Fig. 2 | Comparison with CDM predictions. The contours represent the number density of CDM subhaloes with $M_{\rm sub} > 10^5 h^{-1} M_\odot$. These were obtained using the SASHIMI-C semi-analytical subhalo model[50,51] assuming a host redshift and mass of $z_{\rm h} = 0.881$ and $M_{\rm h} = 10^{12} M_\odot$. The coloured crosses show the $V_{\rm max}$ and $r_{\rm max}$ mean values and 1-σ uncertainties inferred for different models of the detected object: an NFW profile with free concentration (NFW, $\Delta \ln \mathcal{E} = -44$), an NFW halo with concentration drawn from the mass-concentration relation in[28] (NFW$_{\rm CDM,field}$, $\Delta \ln \mathcal{E} = -75$) and an NFW subhalo with concentration drawn from[29] (NFW$_{\rm CDM}$, $\Delta \ln \mathcal{E} = -147$).

https://doi.org/10.1038/s41550-025-02746-w

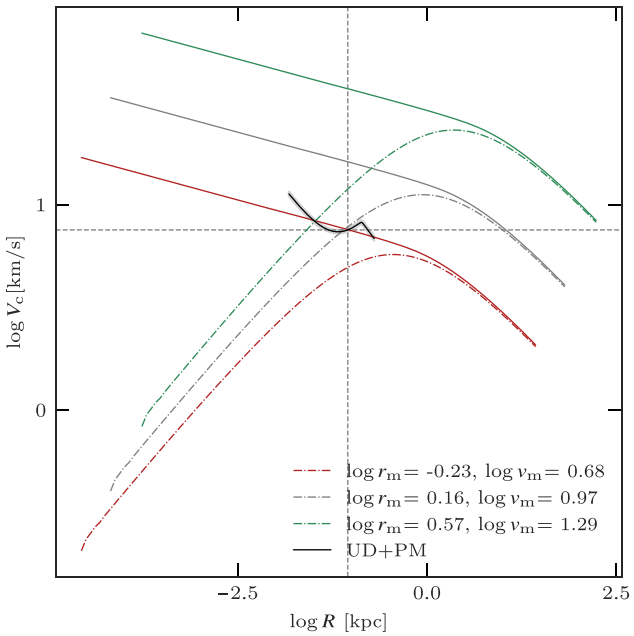

Extended Data Fig. 3 | Comparison with SIDM predictions. Projected 'circular velocity' versus projected radius for different SIDM haloes (solid lines), for their CDM NFW analogues (dashed-dotted lines) and for our best-fit model, a uniform disk with a point mass (UD+PM). The vertical and horizontal lines represent the 90 pc radius at which all models for the detected object agree most closely, and the corresponding circular velocity. The NFW profiles are labelled according to their log values of V_{max} and r_{max}. The uncertainty band in the UD+PM curve represent the 1-σ error around the mean value.

https://doi.org/10.1038/s41550-025-02746-w

Extended Data Table 1 | Macro-model parameters

Parameter	Best fit
κ_0	0.622 ± 0.003
θ [deg]	-18.6 ± 0.2
f	0.811 ± 0.002
x [arcsec]	-0.1234 ± 0.0003
y [arcsec]	-0.1187 ± 0.0004
γ	1.747 ± 0.006
Γ	0.0494 ± 0.0008
Γ_θ [deg]	80.5 ± 0.2
a_3	-0.0046 ± 0.0003
b_3	0.0025 ± 0.0002
a_4	-0.0004 ± 0.0001
b_4	-0.0044 ± 0.0002
$M_{\dagger,A}$ [$10' M_\odot$]	7.83 ± 1.13
x_A [arcsec]	-0.123 ± 0.001
y_A [arcsec]	0.456 ± 0.004

Inferred macro-model parameters, including the mass and position of detection $\mathcal{A}$, for the best-fit case where detection $\mathcal{V}$ is modelled as a uniform disk with a point-mass (UD+PM).